Finite element simulation of welding distortions in ultra-high strength steel S960 MC including comprehensive thermal and solid-state phase transformation models

Ghafouri Mehran, Ahn Joseph, Mourujärvi Juho, Björk Timo, Larkiola Jari

DOI: 10.1016/j.engstruct.2020.110804

Contents lists available at ScienceDirect

Engineering Structures

journal homepage: http://ees.elsevier.com

Finite element simulation of welding distortions in ultra-high strength steel S960 MC including comprehensive thermal and solid-state phase transformation models

Mehran Ghafouri [a,*], Joseph Ahn [b], Juho Mourujärvi [c], Timo Björk [a], Jari Larkiola [c]

[a] Laboratory of Steel Structures, School of Energy Systems, LUT University, P.O. Box 20, 53851 Lappeenranta, Finland
[b] Department of Mechanical Engineering, Imperial College London, South Kensington Campus, London SW7 2AZ, UK
[c] Materials and Production Engineering, Faculty of Technology, University of Oulu, P.O. Box 4200, 90570 Oulu, Finland

ARTICLE INFO

Keywords
Welding simulation
Solid-state phase transformation
Finite element simulation
Ultra-high strength steel
Welding distortion

ABSTRACT

The objective of this study is developing a thermo-metallurgical-mechanical finite element (FE) model incorporating the effect of solid-state phase transformation (SSPT) to accurately simulate deformations for single bead-on-plate welding of an ultra-high strength carbon steel. Comprehensive phase transformation modeling including both diffusive and diffusionless (displacive) transformation kinetics, was performed and the effect of SSPT on welding-induced deformations was investigated. Modelling the heat source and thermal boundary conditions were accomplished in the ABAQUS user subroutines, the former based on the Goldak's double ellipsoidal heat source model. An ABAQUS user subroutine was developed in which kinetics of diffusive and diffusionless transformations based on Machnienko model and Koistinen-Marburger formula, respectively, were implemented. Modification of strains due to volumetric change as a result of SSPT was accomplished using an ABAQUS user-defined subroutine. A comparison between the temperature histories from thermal simulations (with isotropic as well as anisotropic conductivities) and measurement with thermocouples shows that much better verification with experiments can be obtained when anisotropic conductivity is applied. From the results of the mechanical simulations (with and without considering the effect of SSPT) and comparison with measured deformations, it is observable that more accurate prediction of welding-induced angular and bending distortions is possible when the effect of SSPT is incorporated for the material under investigation.

1. Introduction

Indispensable demand of fast-growing technology for light-weight yet high-performance materials has led to advent and actuated the development of ultra-high strength steels (UHSS) as a member of high-strength low-alloy (HSLA) steels during the past decades. Together with high load-bearing capacity, HSLA steels have a superb combination of toughness, weldability and high strength-to-weight ratio making them highly applicable in a wide variety of manufacturing industries such as heavy lifting, oil and gas, automotive and ship-building industries as well as industrial equipment manufacturing sector and offshore construction [1–3].

Cost-effectiveness, efficiency and reliability of fusion welding techniques and in particular, conventional arc welding processes such as gas metal arc welding (GMAW), make them the main and the most prevalent methods of making permanent joints in fabrication of components and structures made up of HSLA steels [1,4]. In this context, dramatic effects of employing such joining techniques operating upon transporting a tremendous heat input into material should be meticulously contemplated. Due to high heat input of arc welding processes and slow cooling rates, HSLA steels in general, experience heat-affected zone (HAZ) softening [5]. The impacts of elevated temperatures on strength reduction of UHSSs, have also been reported [6]. More importantly, rapid non-uniform heating and cooling due to welding thermal cycles, lead to appearance of elasto-plastic thermal strains. SSPT which itself controls thermal and mechanical properties of material and causes localized volume changes, might also arise in the welding area and adjacent HAZ contributing to evolution of thermal strains [7–9]. In addition, inadvertent plastic deformation can degrade performance and quality of the welded connections, impose complexity to assembly of the structure, increase fabrication costs and delay the production and in extreme cases, might cause inapplicability of the entire structure [7,9,10].

Development of well-functioning methodologies and efficient models to predict and analyze welding-induced stresses and strains accurately, become imperative in order to exploit the maximum load-bearing capacity of the joints made up of UHSSs and provide safety to their application. In this regard, FE method has proven its potential and reliability to solve a broad spectrum of linear and non-linear mathematical and engineering problems. In the field of heat transfer and welding simulations, over the past decades, computational welding mechanics (CWM) aiming at analyzing the temperature field, welding-induced stresses and strains along with microstructural evolution has been significantly developed [11–16]. Numerous studies have been hitherto conducted concern-

* Corresponding author.
E-mail address: mehran.ghafouri@lut.fi (M. Ghafouri)

https://doi.org/10.1016/j.engstruct.2020.110804
Received 11 November 2019; Received in revised form 5 April 2020; Accepted 12 May 2020
Available online xxx

ing welding simulation and prediction of residual stresses and distortions for different joint types [4,10,17–19], materials [4,10,18–25] and welding processes [4,10,19,24]. Although remarkable research has been devoted to welding simulation of steels, a few concentrated on comprehensive metallurgical modeling [26,27]. With respect to high strength steels (HSS) and UHSSs, some studies considered welding simulations including austenite–martensite transformation [25,28–30] and some neglected such effect [24]; however, less attention has been paid to comprehensive metallurgical modelling including both diffusive and displacive transformations for modern direct-quenched thermo-mechanically rolled UHSSs. Accurate prediction of welding deformations is essential in decreasing fabrication costs, increasing the quality and performance of the joint, service life of the component as well as efficiency of production processes such as digitalized robot welding. The objective of this research is developing a comprehensive thermo-metallurgical-mechanical (TMM) FE model to accurately predict welding-induced angular and out of plane bending distortions of direct-quenched thermo-mechanically rolled UHSS S960 MC. In this regard, a three-dimensional sequentially-coupled model for numerical simulation of a single pass bead-on-plate welding of the UHSS S960 MC specific to GMAW process is elaborated in ABAQUS software [31].

Accurate computational modeling of thermal and metallurgical phenomena which incorporates both diffusive and displacive SSPT kinetics models in FE simulation is accomplished. Subsequently, the effect of SSPT on mechanical analysis and prediction of out of plane angular and bending deformations are investigated. Thermal phenomena is modeled by applying a body heat flux upon implementation of Goldak's double ellipsoidal heat source model [32] in the user subroutine DFLUX and developing the user subroutine FILM to consider the combined convective and radiative heat transfer. Dilatometric tests are conducted and continuous cooling transformation (CCT) diagram of the material is determined experimentally. A linear relationship to consider incomplete austenite transformation during heating based on the previous researches [26,28,33] along with Machnienko kinetics for diffusional and Koistinen-Marburger equation for diffusionless transformations are implemented in the user subroutine USDFLD. Volume fractions of austenite during heating as well as arising phases upon austenite decomposition in cooling stage are accordingly calculated. The computed volume fractions together with experimentally obtained full volumetric change strains from dilatometric data are formulated in the user subroutine UEXPAN to calculate volume changes due to phase transformation during both heating and cooling. Computer simulations in terms of prediction of temperature histories, present microconstituents in fusion zone (FZ) and HAZ as well as welding-induced distortions are verified by experimental measurements.

2. Experimental procedure

2.1. Material

The parent material used in this study is S960 MC manufactured by SSAB, which is an advanced low carbon ultra-high strength low alloy steel offering a minimum yield strength of 960 MPa. This UHSS is made by a modern thermo-mechanical rolling process integrated with direct quenching in which water quenching occurs forthwith after hot rolling. This process differs from the conventional method, which contains hot rolling, air-cooling, reheating and ultimately quenching [34,35].

The filler material utilized to deposit the weld bead is Böhler Union X96 solid wire with 1 mm diameter, which practically has the same strength as the parent material [36]. Chemical composition of the material under investigation based on the material certificate of the manufacturer and those of filler material from the literature [37] are presented in the table 1.

2.2. Welding procedure

A single rectangular block of S960 MC with dimensions of 300 × 300 × 8 mm was used as the base material upon its center line, a layer of filler material in a single pass GMAW process was deposited. It must be mentioned that base material was positioned in the way that welding torch travels in transverse direction (perpendicular to rolling direction) of the material. The convention for welding direction was assumed to be along the $+Y$-axis and $+Z$ is normal to the top surface of the plate. Welding was carried out in ambient temperature of 20 °C without any application of preheat based on the recommendation of the manufacturer [38]. Due to softening effects on the material, heat input level should be optimized [36], thus, welding parameters were adjusted to meet the heat input requirements, as are presented in the table 2.

Adjusting the value of 0.8 as the welding efficiency for GMAW process, a total energy of 179.2 kJ corresponding to a net heat input value of 640 J/mm was supplied during the welding.

2.3. Temperature measurement

Temperature histories during welding were monitored by attaching several K-type thermocouples at different positions on top as well as bottom surfaces of the parent material. It is worthy of note that as long as the FE model is verifiable by experimental results, the choice of number and location of thermocouples are optional. Two thermocouples were detached during welding and failed to record the temperature. The positions at which six thermocouples were mounted are schematically shown in Fig. 1. Thermocouples T_1 and T_4 attached in HAZ to capture higher temperatures while T_2 and T_3 mounted in base material, show lower temperatures. B_1 and B_2 provide more data regarding the temperature distribution through thickness. From FE point of view, six thermocouples can provide sufficient data to verify the nodal temperatures calculated by FE model.

2.4. Deformation measurement

Out of plane angular and bending distortions on specified paths on top surface before and after welding were measured using the laser profile scanner Micro-Epsilon optoNCDT 1700–20 in order to compare with numerical simulation as are depicted in Fig. 2. Paths 1 & 2 (red solid lines) starting at the weld toe, demonstrate the paths along which angular distortion is measured.

Table 1
Chemical compositions of S960 MC and Böhler Union X96 (wt. %).

Material	C	Si	Mn	P	S	Al	Ti	Cu	Cr	Ni	Mo	N
S960 MC	0.097	0.20	1.09	0.008	0.001	0.034	0.02	0.033	1.13	0.38	0.191	0.005
Union X96	0.12	0.80	1.90	–	–	–	–	–	0.45	2.35	0.55	–

Table 2
Welding process parameters.

Voltage (V)	Current (A)	Travel speed (m/min)	Wire diamater (mm)	Wire feed rate (m/min)	Gas flow rate (L/min)	Tip distance (mm)	Shielding gas
28	200	0.42	1	10	19.3	18	92% Ar + 8% CO2

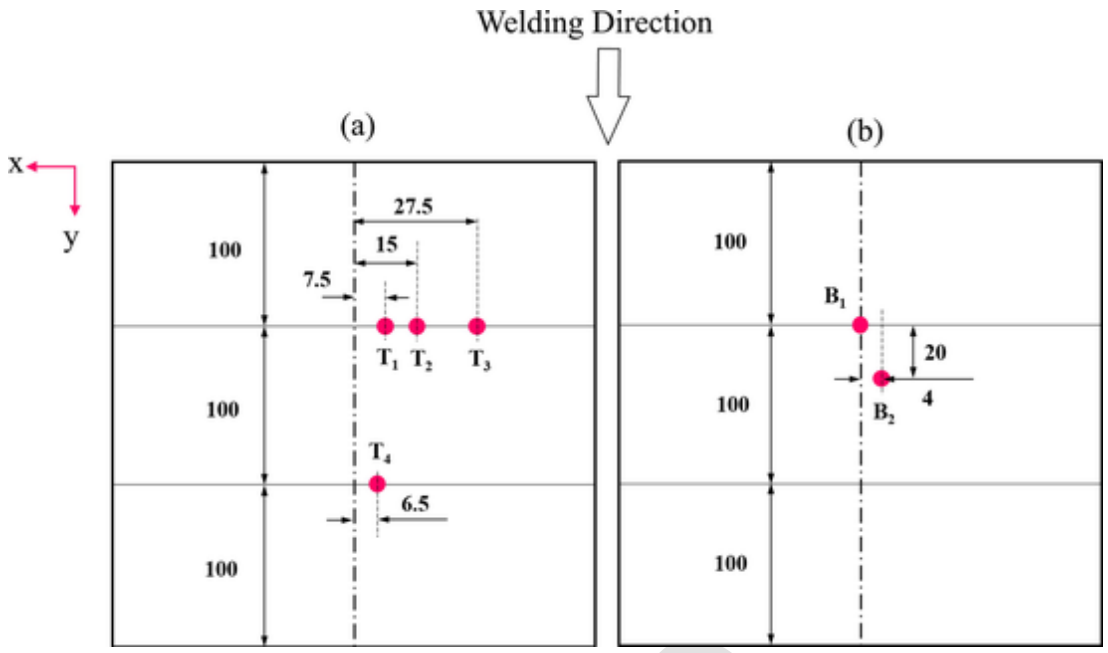

Fig. 1. Positions of thermocouples on top (a) and bottom (b) surfaces. (Units in mm).

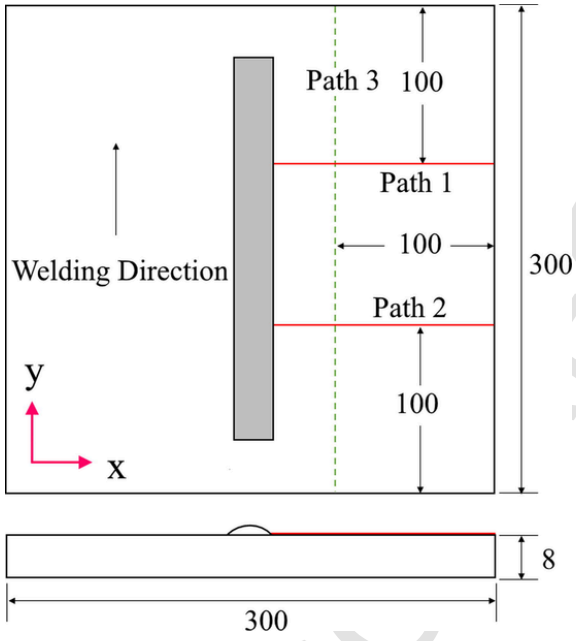

Fig. 2. Measurement paths for angular and bending distortions. (Units in mm).

Path 3 (green dashed line) shows the measuring path for out of plane bending distortion.

3. Finite element simulation

Welding is a complex joining process which includes coupled interactions between heat and mass transfer, microstructural alterations and evolution of mechanical fields. Numerical procedures to accurately simulate such process, can be highly complicated and might not reach realistic solutions especially if capturing all the aspects is concerned. Not all the factors that impose complexity to welding simulation are consequential and thus, simplification of presumptions will result in elaborating an efficient yet precise model [20,28].

FE method is adopted to simulate the welding process and investigate the evolution of microstructure and development of distortions due to existence of a transient thermal field during welding in the current study. Capturing the temperature histories, simulation of phase transformation and prediction of welding distortions are accomplished developing a sequentially-coupled TMM formulation in ABAQUS FE code. Sequentially-coupled analysis is stated to have a favorable performance as dimensional changes during welding are insignificant and the effect of structural response on thermal field is inconsequential [4,25]. In thermal analysis, non-linear transient temperature field due to a moving heat source is determined upon solving constitutive heat conduction equation subject to defined boundary conditions. Metallurgical analysis is performed by calculating the volume fractions of austenite in heating and arising phases in cooling. In the subsequent mechanical analysis, the temperature histories obtained in the previous steps, are applied as thermal load. In addition, volume changes due to phase transformations are used to modify the thermal expansion coefficients and find the structural response and calculate the displacements at nodes.

3.1. Model geometry and FE mesh

Modeling the as-welded geometry was carried out by extracting the curvature of the weld bead from the macrosection of the weld seam. Due to symmetry concerning the weld center line, only one-half of the geometry was considered as the analysis domain. Inasmuch as nodal temperatures captured in thermal analysis need transferring into the model for mechanical analysis, the same FE mesh with identical time steps as is shown in Fig. 3, albeit, with different element types were used in both analyses.

Respecting element types in welding simulation problems, employment of linear brick elements for both thermal and mechanical analyses by some authors [21,25] and application of quadratic brick elements in thermal as well as mechanical analyses [24] have been reported. Ahn et al. [19] on the other hand, used quadratic brick elements in thermal analysis and linear brick elements in the subsequent mechanical analysis. Thermal analysis in the present study, however, was performed by employing linear hexahedral eight-node three-dimensional continuum diffusive heat transfer elements (DC3D8) with temperature as the only degree of freedom at each node. Heat transfer analyses involving latent heat effects, as is incorporated in this study, are preferred to be solved using first order diffusive elements owing to their special integration approach [31]. First order reduced integration hexahedral three-dimensional continuum elements (C3D8R) with three translational degrees of freedom at each node were used in mechanical analysis. A better convergence is supposed to be achieved and excessive locking is prohibited during mechanical analysis using reduced integration elements [28].

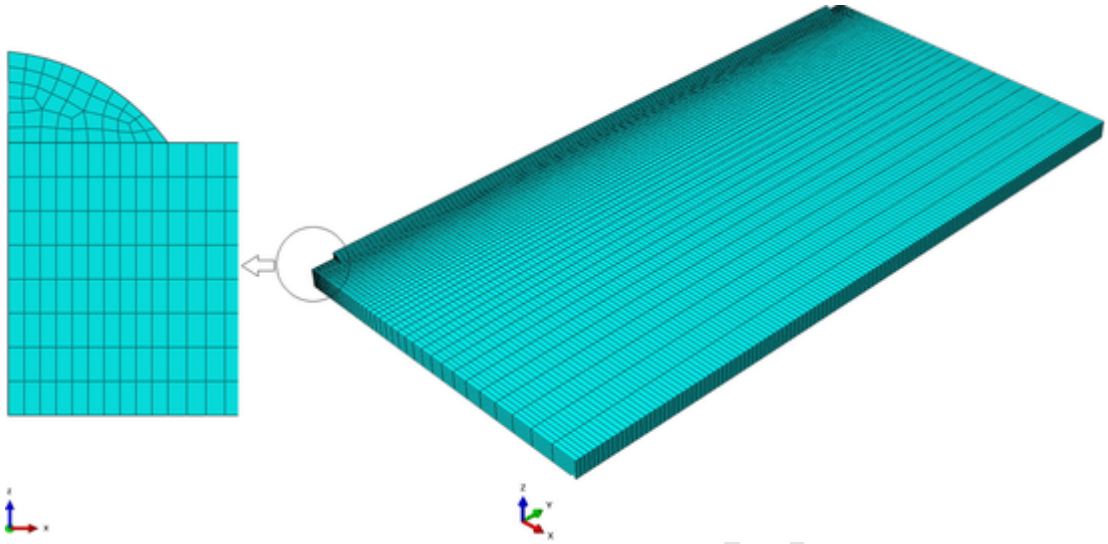

Fig. 3. Meshed symmetric geometry used in the analysis.

A fine mesh grid in FZ and its close vicinity was applied, which becomes coarser as the distance towards the edges in transverse to welding direction increases. Fine mesh ensures accurate application of a heat flux introduced by a travelling torch which causes high temperatures and dramatic stress gradient in FZ and HAZ [19,28]. Mesh sensitivity was analyzed to study the effect of mesh density on the accuracy of the results. Mesh convergence was approached when no more accuracy was rendered by further mesh refinement. By taking into account the computational costs, a fine mesh with a total number of 64,808 elements and 71,398 nodes and the smallest element size of 2.8 × 0.5 × 0.5 mm was found sound enough to provide more than sufficient accuracy to the results.

3.2. Temperature-dependent material properties

Temperature-dependent thermo-physical properties of the base and filler materials namely density (ρ), thermal conductivity (k) and specific heat (c) were obtained as a function of their chemical compositions from JMatPro [39]. In this study, due to very similar thermo-physical properties of the base and filler materials, they were defined as the same material and those of base metal was used for both materials as are shown in Fig. 4. It is worthy to mention that units are arranged so that all the properties can be shown in one single graph.

With respect to mechanical properties of material, temperature-dependent Poisson's ratio (ν) was taken from JMatPro [39]. Temperature-dependent yield strength and Young's modulus of base metal were experimentally obtained through conducting hot tensile tests from room temperature (RT) up to 1200 °C. True stress–strain curves of the base material at tested temperatures are shown in Fig. 5. Owing to difficulty finding those of filler material especially at high temperatures, mechanical properties of filler metal were assumed identical to those of base metal as are shown in Fig. 6.

3.3. Thermal analysis

Transient temperature field during welding is defined by constitutive heat conduction equation derived from Fourier's law of heat conduction and law of energy conservation with temperature-dependent material characteristics:

$$\rho(T)\,c_p(T)\,\frac{\partial T}{\partial t} = \frac{\partial}{\partial x}\left(k(T)\,\frac{\partial T}{\partial x}\right) + \frac{\partial}{\partial y}\left(k(T)\,\frac{\partial T}{\partial y}\right) + \frac{\partial}{\partial z}\left(k(T)\,\frac{\partial T}{\partial z}\right) + \dot{Q}_v \tag{1}$$

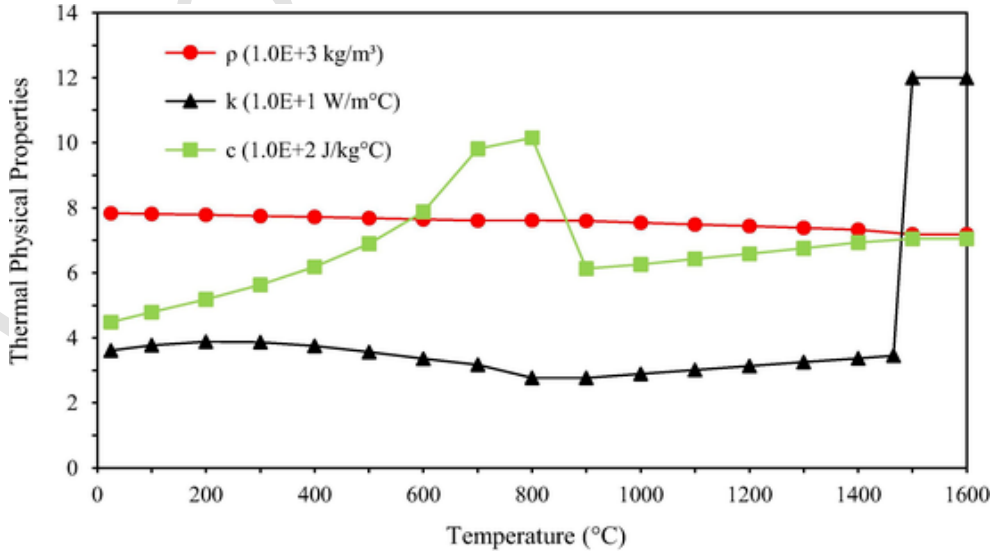

Fig. 4. Temperature-dependent thermo-physical properties of S960 MC.

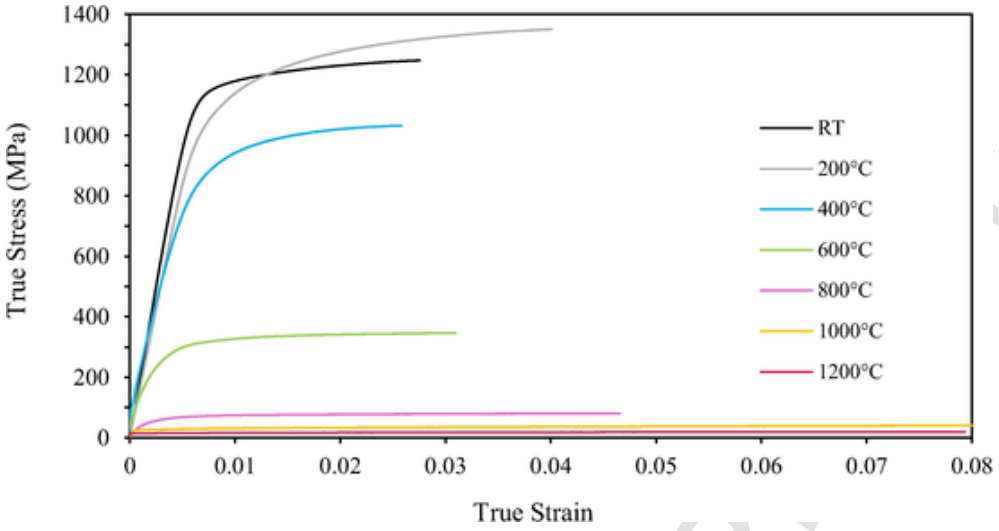

Fig. 5. True stress-strain curves of S960 MC at different temperatures.

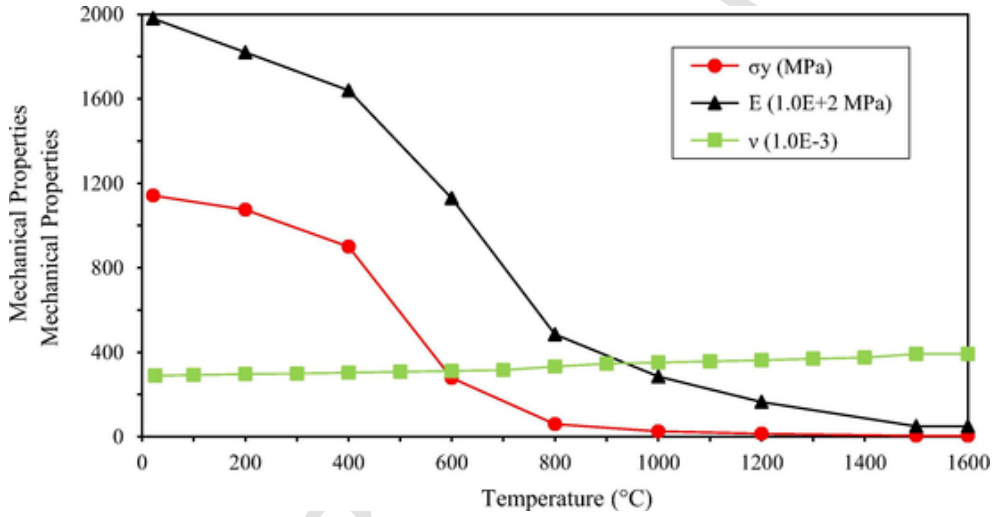

Fig. 6. Temperature-dependent mechanical properties of S960 MC, σ_y (yield strength), E (modulus of elasticity) and ν (poisson's ratio).

where $\rho(T)$ [kg/m^3], $c_p(T)$ [J/kg°C] and $k(T)$ [W/m°C] are temperature-dependent density, specific heat and thermal conductivity, respectively. T [°C] is temperature and t [s] represents time. $\dot{Q}_v$ [W/m^3] is known as volumetric heat source density or internal volumetric heat generation rate. In the present work, arc energy from a moving heat source transferred to the parent and weld metals, was applied as a volumetric heat flux implemented in the ABAQUS user subroutine DFLUX based on the model with double ellipsoidal distribution elaborated by Goldak et al. [32]. The model describes two heat flux distributions, one for the front half of the heat source:

$$q_f(x,y,z,t) = \frac{6\sqrt{3}f_f Q}{ab_f c\pi\sqrt{\pi}} e^{-3\left(\frac{x^2}{a^2}+\frac{[y-vt-y_0]^2}{b_f^2}+\frac{z^2}{c^2}\right)}, y \geq 0 \quad (2)$$

Similarly, for the rear half:

$$q_r(x,y,z,t) = \frac{6\sqrt{3}f_r Q}{ab_r c\pi\sqrt{\pi}} e^{-3\left(\frac{x^2}{a^2}+\frac{[y-vt-y_0]^2}{b_r^2}+\frac{z^2}{c^2}\right)}, y<0 \quad (3)$$

where x, y, z are coordinates in the reference system. Q is power of the welding arc which is calculated using arc voltage, current and welding efficiency η, is assumed to be 0.8 for GMAW process [20]. The parameters a, b_f, b_r and c are Goldak's weld pool characteristics which can be initially adopted based on the photomacrograph of weld cross-section and weld pool boundaries dimensioning [11]. Via iteration, those parameters can be precisely adjusted to reach a favorable molten zone and a close agreement between temperature histories from simulation and experiment. f_f and f_r are dimensionless fractions of the heat deposited in front and rear half of the heat source, respectively. Heat source parameters and their values used in the analysis, are summarized in the table 3. The following mathematical relationships are observable by taking the continuity of the heat source into account:

$$\frac{f_r}{b_r} = \frac{f_f}{b_f} \quad (4)$$

$$f_f + f_r = 2 \quad (5)$$

Integration process will be involved in solving the Eq. (1) in which an arbitrary constant will be inserted. A unique solution will be found if the specific

Table 3
Parameters of Goldak's heat source model.

Parameter	a(mm)	b_f(mm)	b_r(mm)	c(mm)	f_f	f_r
Value	4.6	5	14	4	0.53	1.47

boundary conditions are defined. The most frequently applied boundary conditions in welding simulations are heat losses due to convection and radiation from free surfaces being defined based on the Newton's law of cooling and Stefan-Boltzmann's law, respectively. The involvement of the mentioned phenomena in this study was fulfilled by considering the combined effect of convection and radiation, which is represented via the two mathematical expressions in the Eq. (6) as was practiced by several researchers [4,40,41]. The user subroutine FILM in ABAQUS was developed to model the combined thermal boundary conditions.

$$h = \begin{cases} 0.0668 \times T \quad (\frac{W}{m^2{}^\circ C}) & 0 \leqslant T \leqslant 500 \\ 0.231 \times T - 82.1 \quad (\frac{W}{m^2{}^\circ C}) & T \geqslant 500 \end{cases} \tag{6}$$

where h denotes the temperature-dependent heat transfer coefficient.

In the context of thermal simulation and calibration of model, convective stirring effect of fluid flow in molten zone was modeled using artificially increased thermal conductivity in temperature ranges higher than melting point termed as effective heat conductivity due to thermo-capillary flow, which is also known as Marangoni effect [4,28,40]. In this regard, thermal conductivity increased linearly between solidus and liquidus temperatures by a factor of three compared to the value of ambient temperature. Latent heat of fusion was taken into account to model the heat effects of solidification in weld pool by assuming the value 260 × 10^3 J/kg between solidus temperature 1465 °C and liquidus temperature 1520 °C.

3.3.1. Incorporation of anisotropic heat conductivity in thermal analysis

As mentioned above, with regards to calibration of thermal model to reach an agreement between temperature histories from simulation and experiment, different parameters such as heat source parameters can be calibrated. As will be shown in the results section, further calibration of thermal model (in addition to calibration of Goldak's parameters) to reflect accurate temperature field comparable with experiment, was only possible when anisotropic temperature-dependent thermal conductivity was defined as a calibrating tool. Different phenomena might be involved whose effects were taken into account using anisotropic conductivity. One possible hypothesis is introduced based on the measurement of pre-austenite grain structure of the material and available literature connecting size of grains to anisotropic conductivity. Rolled steel sheets are believed to show orthotropic behavior [42]. Production process of steels can cause alteration in their spatial organizations and size of grains in different directions and anisotropy as a result. The mechanism is not discussed here but it is considered as a known priori. In a study by Jonšta et al. [43], effect of grain size on conductivity of steel samples was investigated. Improved heat transfer and higher thermal conductivity through the coarse-grained samples owing to a fewer number of grain boundaries implying less barrier and reduced resistance versus heat conduction, was reported. Austenite morphologies of the material under investigation in rolling (RD), transverse (TD) and normal (ND) directions is depicted in Fig. 7.

As can be seen in Fig. 7 in RD-ND section, grains are elongated in RD while considerably compressed in ND. A similar pattern is observable in section TD-ND. Size of grains in RD, TD and ND were measured approximately 60.9 μm, 50.6 μm and 11 μm, respectively [44]. Based on this hypothesis, smaller grain size in ND might have an effect on weakening the thermal conductivity through thickness. In this regard, anisotropic material was defined in ABAQUS to which in thickness direction, decreased heat conductivity values compared to those of rolling and transverse directions, in the entire temperature ranges below the austenitization temperature, were assigned. Those values, then, were iterated to reach a close agreement between the temperature histories predicted by simulation and experiment as are summarized in the table 4.

3.4. Mechanical analysis

In a sequentially-coupled formulation, temperature histories predicted in thermal analysis are used as thermal load in mechanical analysis. Mechanical (structural) analysis is accomplished upon solving non-linear elasto-plastic governing partial differential equations. One of the equations is equilibrium equation [45]:

$$\nabla.\sigma + F_b = 0 \tag{7}$$

where ∇ is divergence operator, σ shows Cauchy stress tensor and F_b implies body force vector. The other equation is thermal elasto-plastic constitutive equation through which the relation between stresses and strains is expressed [46]:

$$\{d\sigma\} = [D]\{d\varepsilon\} - \left[C_{th}\right]\{dT\} \tag{8}$$

And $[D] = [D^e] + [D^p]$

where $d\sigma$, $d\varepsilon$ and dT show increments of stress, strain and temperature, respectively. C_{th} is matrix of thermal stiffness, $[D^e]$ and $[D^p]$, respectively denote elastic and plastic stiffness matrices. Taking the effect of SSPT into account, the total strain rate component in this study, is decomposed by its constituents as is expressed by Eq. (9):

$$\dot{\varepsilon}^{total} = \dot{\varepsilon}^e + \dot{\varepsilon}^p + \dot{\varepsilon}^{th} + \dot{\varepsilon}^{\Delta V} \tag{9}$$

where $\dot{\varepsilon}^{total}$ is total strain rate. $\dot{\varepsilon}^e$, $\dot{\varepsilon}^p$ and $\dot{\varepsilon}^{th}$ correspond to elastic, plastic and

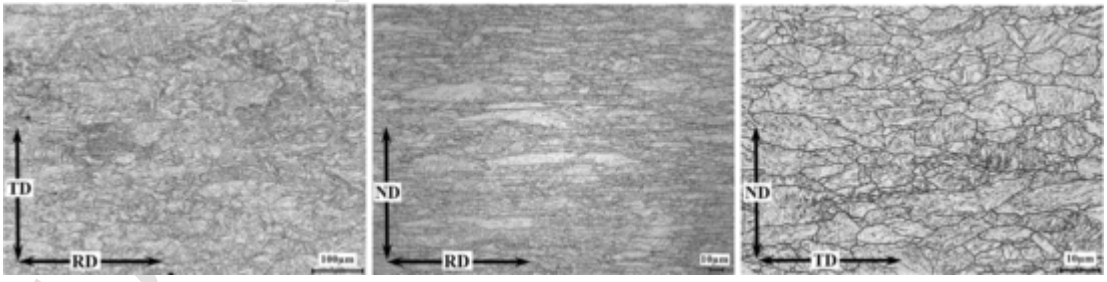

Fig. 7. Pre-austenite grain structure of S960 MC [44].

Table 4
Anisotropic thermal conductivity values used in thermal analysis.

Temperature (°C)		25	200	400	600	800	1000	1200	1400	1500
Thermal conductivity (W/m°C)	RD	36	39	37	34	28	29	31	34	120
	TD	36	39	37	34	28	29	31	34	120
	ND	16	20	19	18	15	29	31	34	90

thermal strain rate components, respectively. $\dot{\varepsilon}^{\Delta V}$ is volumetric change strain due to phase transformation. Elastic strain is calculated using inverted generalized Hook's law in which temperature-dependent Poisson's ratio and Young's modulus are applied as below:

$$\varepsilon_{ij}^{e} = \frac{1}{E}\left[(1+\nu)\sigma_{ij} - \nu\sigma_{kk}\delta_{ij}\right] \tag{10}$$

where δ_{ij} is Kronecker delta, E represents Young's modulus, ν indicates Poisson's ratio and σ_{ij} is stress tensor. Plastic strain component is calculated upon employing a rate-independent plastic model as is demonstrated in Eq. (11), with temperature-dependent mechanical properties, Von Mises yield surface and isotropic hardening model [47]:

$$\dot{\varepsilon}_{ij}^{p} = \lambda s_{ij} \tag{11}$$

And $s_{ij} = \sigma_{ij} - \frac{1}{3}\sigma_{kk}\delta_{ij}$ where $\dot{\varepsilon}_{ij}^{p}$ is plastic strain rate component, λ signifies the plastic flow factor and s_{ij} represents the deviatoric stress tensor, which is calculated by subtracting the hydrostatic tensor from the total stress tensor. The present study considers the effect of annealing on plastic behavior of material. When temperature of material rises and exceeds a specific temperature called annealing temperature, strain hardening memory is annihilated and the effect of prior work hardening for that node is removed. This matter is accomplished by ABAQUS through resetting the equivalent plastic strain to zero. On condition that a nodal temperature of material falls below the defined annealing temperature, it can work harden again [19,28]. The implementation in ABAQUS was performed via defining a sub-option in plastic properties of material which was set to a value of 900 °C in mechanical analysis. A cut-off temperature of 1500 °C was defined for material properties in mechanical analysis. If temperature exceeds 1500 °C, material properties are evaluated at cut-off temperature. In order to avoid convergence difficulties, yield strength and Young's modulus values at cut-off temperature were reduced to 5 MPa and 5GPa, respectively. Inasmuch as no special clamping was used to constrain the work piece, in structural analysis, boundary conditions were defined to solely prevent rigid body motion [33]. That is, the symmetry plane is restricted in *X*-direction. Point *A*, the first node lying on welding centerline is constrained in *Y* and *Z*-directions and the last point on the welding centerline, point *B*, is restricted to move in *Z*-direction as is shown in Fig. 8.

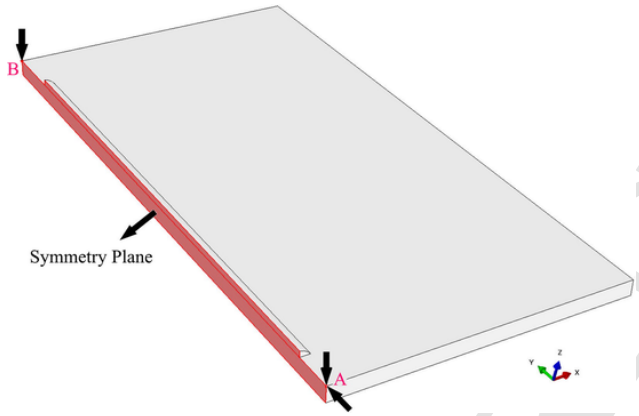

Fig. 8. Mechanical boundary condition.

3.5. Solid-state phase transformation

Involvement of volumetric change strain component in calculation of total strain increment was accomplished using the analysis of SSPT by applying kinetics of phase transformation and CCT diagram. Kinetics of SSPT was defined using applied mathematical models in which dilatometric data concerning the present phases during heating and cooling, transformation temperatures, linear thermal expansion coefficients of microconstituents as well as full volumetric change strains of present phases were mathematically correlated. All the data required to express transformation kinetics models in this study, were experimentally obtained by conducting dilatometric tests. An experimental graph regarding the heating rate 640 °C/s and cooling rate 50 °C/s is shown in Fig. 9. Thermal cycles during welding are addressed to as the particular contributor in occurrence of SSPT and associated volume change in steels. Volumetric change strains induced by transformations were derived from phase work hardening owing to the difference in thermal expansion coefficients of present phases [19].

3.5.1. Austenitic transformation model

Prior to undergoing any thermal cycle, microstructure of the base material, based on Scanning electron microscopy (SEM) image, as is shown in Fig. 10, is a mixture of bainite and martensite.

When material is heated up to A_1 temperature, bainitic-martensitic microstructure of base metal starts to transform to austenite with a decrease in its net volume. It is assumed that increase in the volume fraction of austenite be-

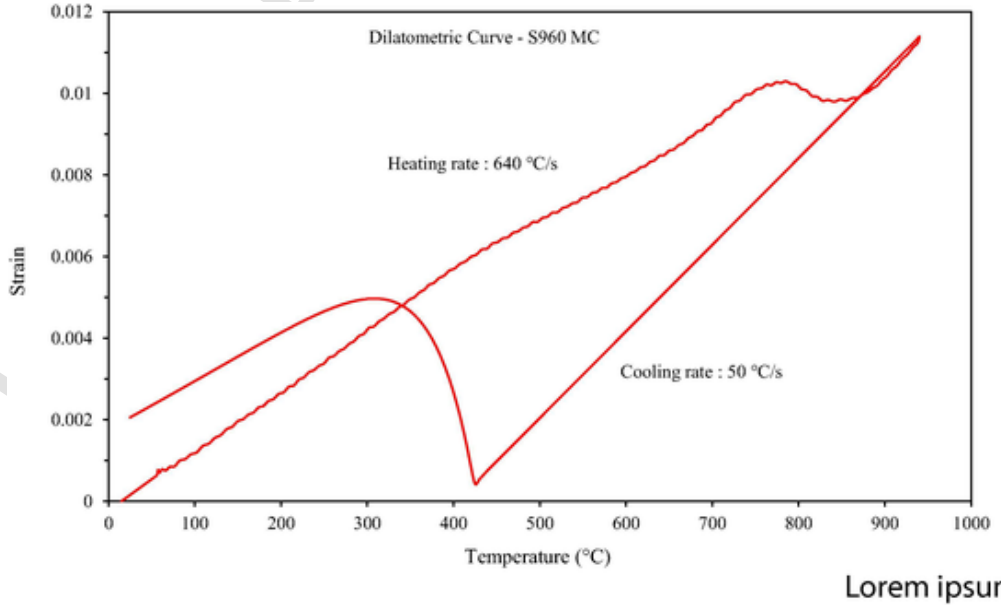

Fig. 9. Dilatometric curve of the investigated material for heating rate 640 °C/s and cooling rate 50 °C/s.

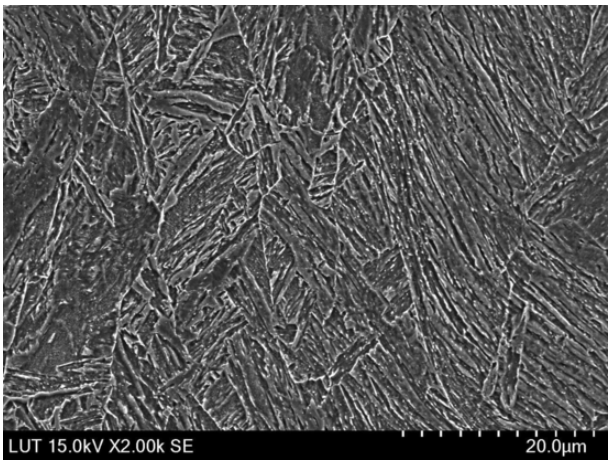

Fig. 10. Scanning electron micrograph of S960 MC with bainite and martensite as microconstituents.

tween A_1 and A_3 temperatures in heating, follows a linear rule as follows [26]:

$$f_a = \frac{T_{\max} - A_1}{A_3 - A_1}$$
$$A_1 \le T_{\max} \le A_3 \tag{12}$$

where f_a denotes the volume fraction of austenite during austenitic transformation as a function of $T_{\max}$, the maximum temperature a material point meets during heating. A_1 and A_3 which are lower and upper critical temperatures, respectively, were determined based on the analysis of the experimental dilatometric curve during heating and application of tangent-intersection method as was practiced by Li et al. [48]. The values of 775 °C and 863 °C were obtained for A_1 and A_3 temperatures, respectively.

3.5.2. Diffusive transformation model

In diffusional transformation, might exist one or more nascent phases whose chemical compositions differ from the extant parent phase which requires long-distance diffusion. As the name indicates, the most substantial factor in this transformation is thermally activated atomic diffusion or movement of individual atoms. Inasmuch as diffusion is a time-dependent phenomenon, such transformations are not instantaneous and occur in the course of time [49]. Volume fractions of phases whose transformations from austenite in cooling is diffusional, were defined using the final fraction of that specific microstructural constituent which depends on the cooling rate in the range 800–500 °C ($V_{8/5}$) in addition to start and ending transformation temperatures. For the material under investigation, bainite is the only microconstituent whose formation is defined upon the kinetics of diffusive transformation based on the prevalent cooling rates in HAZ. Final fraction of bainite was calculated from the experimentally-determined CCT diagram. Kinetics model of Machnienko for diffusive transformation was applied as was previously practiced by Piekarska et al. [23] :

$$f_b(T,t) = f_b^{\%} f_a \left[1 - exp\left(-k_a \frac{B_s - T}{B_s - B_f}\right)\right]$$
$$B_f \le T \le B_s \tag{13}$$

where $f_b(T,t)$ denotes the volume fraction of bainite during diffusive transformation as a function of T, current temperature. f_a is the volume fraction of austenite formed during heating and $f_b^{\%}$ is the final fraction of bainite determined based on the CCT diagram which is shown in Fig. 11. k_a is a factor whose value was adjusted in the range 2.5–3. Bainite start temperature (B_s) and bainite finish temperature (B_f) were experimentally obtained from dilatometric tests being respectively 520 °C and 460 °C in both FZ and HAZ.

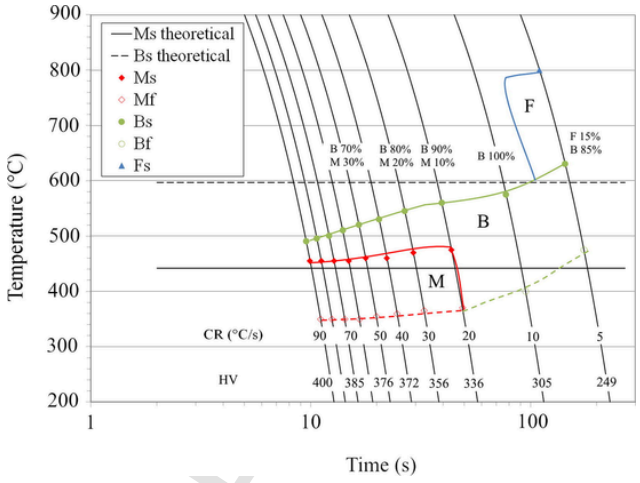

Fig. 11. CCT diagram of S960 MC.

3.5.3. Martensitic transformation model

Diffusionless or displacive transformation refers to a transformation in which chemical composition of the nascent phase remains identical to extant parent phase. In steels, transformation of martensite from austenite has a diffusionless nature in which chemical composition of austenite is directly inherited by martensite [33,49]. Transformation of martensite from austenite, analogous to bainite transformation is followed by an increase in net volume. The amount of martensite transformed from austenite in cooling, depends highly on the martensite start temperature (M_s), which is the onset of transformation of austenite into martensite. Martensite transformation is presumed to be completed when martensite finish temperature (M_f) is met. M_f is the temperature at which austenite is fully transformed to martensite and below which, further cooling has no effect on amount of the formed martensite [25]. M_s and M_f temperatures were identified experimentally based on the dilatometric curves during cooling which were set to 460 °C and 355 °C, respectively. Tracking the volume fraction of martensite during cooling in the temperature ranges below M_s, were accomplished by employing Koistinen-Marburger kinetics model [23] as is expressed in the following formulation:

$$f_m = f_m^{\%} f_a \left[1 - exp\left(-k_m \left(M_s - T\right)\right)\right]$$
$$M_f \le T \le M_s \tag{14}$$

where f_m denotes the volume fraction of martensite during martensitic transformation at T, current temperature. $f_m^{\%}$ is the final fraction of martensite obtained from the CCT diagram. Transformation evolution is characterized according to temperature by the factor k_m which was considered 0.05 in the present study based on the recommendations of Li et al. [30]. The sum of the strains due to thermal expansion and volume change in Eq. (9) is referred to as thermal dilatation which is calculated from the following expression [23]:

$$d\varepsilon^{th+\Delta V} = d\varepsilon^{th} + d\varepsilon^{\Delta V} = \sum_i \alpha_i f_i dT - sign(dT) \sum_i \varepsilon_i^{\Delta V *} df_i \tag{15}$$

where f_i indicates the volume fraction of phase i calculated from Eqs. (12), (13) and (14) whereas, df_i shows the derivative of the mathematical expressions to calculate volume fraction of phase i. α_i shows linear thermal expansion coefficient of phase i. The values of α_a, α_b and α_m corresponding to austenite, bainite and martensite in the present study, based on the dilatometric curves are 2.02, 1.25 and 1.37 ($\times 10^{-5}$) $\left[\frac{1}{°C}\right]$. The full volumetric change strain $\varepsilon_i^{\Delta V *}$ of phase i due to full austenitic, bainitic and martensitic transformations were determined based on dilatometric curves. The values 1.51, 4.10 and 6.6 ($\times 10^{-3}$) were respectively assigned to austenite, bainite and martensite. *Sign* function depends on temperature change, i.e. provided that temperature difference is

positive which happens during heating, $sign$ is equal to $+1$ and during bainitic and martensitic transformations is equal to -1 [23].

3.5.4. Implementation of SSPT in ABAQUS

Simulation of phase transformation and modification of strains in mechanical analysis, were performed by implementation of SSPT kinetics in numerical subroutines in ABAQUS. User subroutine USDFLD is generally utilized to define material properties at each integration point of an element as a function of field variables. ABAQUS Utility routine GETVRM inside the USDFLD is used to access a material point data [31]. That is, temperature changes between the increments are saved inside a field variable. Based on the sign of temperature change (positive during heating and negative in cooling) and the maximum temperature of each integration point which was recorded by GETVRM, different scenarios are deemed and the decision is made whether or not the point has undergone transformation. For the material points underwent transformation, the relevant kinetics model is applied to obtain volume fraction of austenite during heating and arising phases upon the austenite decomposition in cooling [20,23,26]. In this context, to obtain volume fractions of microstructural constituents at each node and time increment, Eqs. (12), (13) and (14) were implemented in USDFLD subroutine. Solution-dependent state variables (SDVs) in USDFLD subroutine were employed in order to store the calculated volume fractions based on the above-mentioned mathematical relationships. SDV5, SDV7 and SDV8 are state variables in which calculated volume fractions of base material, bainite and martensite are respectively stored. A descriptive diagram regarding the implementation of the phase transformation kinetics in USDFLD is provided in Fig. 12. User subroutine UEXPAN is employed in applications where incremental thermal strains are defined as a function of temperature, field variables or state variables [31]. The output of USDFLD saved in field variables and state variables, are passed into the UEXPAN where incremental strains according to Eq. (15) are modified [23,26].

4. Results and discussion

4.1. Validation of thermal analysis

Distribution of temperature during welding based on the numerical simulation incorporating anisotropic temperature-dependent thermal conductivity is shown in Fig. 13. The Peak temperature calculated in the thermal analysis falls within the realistic temperature ranges (1800–2200 °C) based on the reported results by other researchers for similar welding process [4,25].

Prediction of the shape and size of the weld pool might act as an auxiliary index of correct thermal distribution in FZ and HAZ supplementary to temperature history records. Determining the precise weld pool shape and boundaries, requires modeling the fluid flow and dynamics of weld pool, which is not the concern of this study. In this regard, however, Goldak's parameters were adjusted in a realistic manner so that reinforcement width and depth of penetration are in close concurrence with the experimentally observed ones. A comparison has been drawn between the simulated and measured width and length of the fused reinforcement on top surface at the end of welding path in Fig. 14

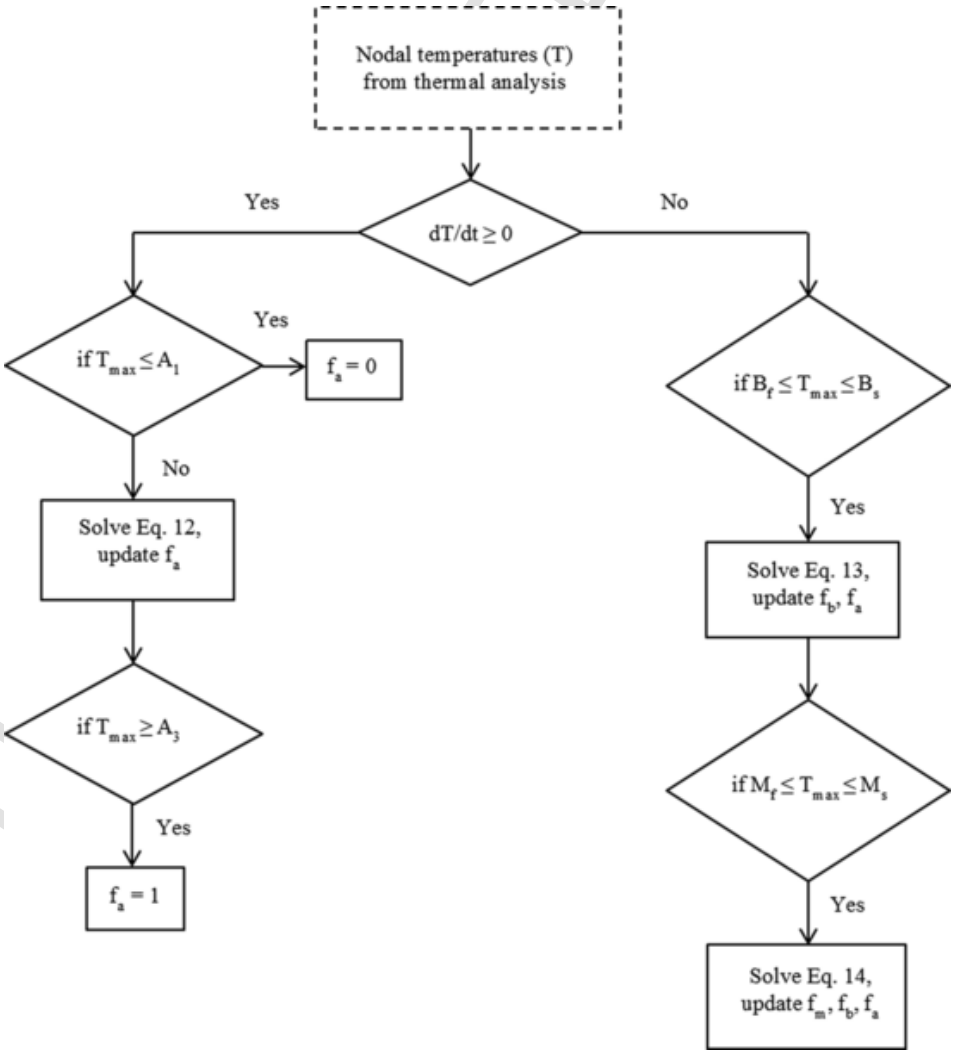

Fig. 12. The flow diagram of implanting SSPT kinetics in USDFLD.

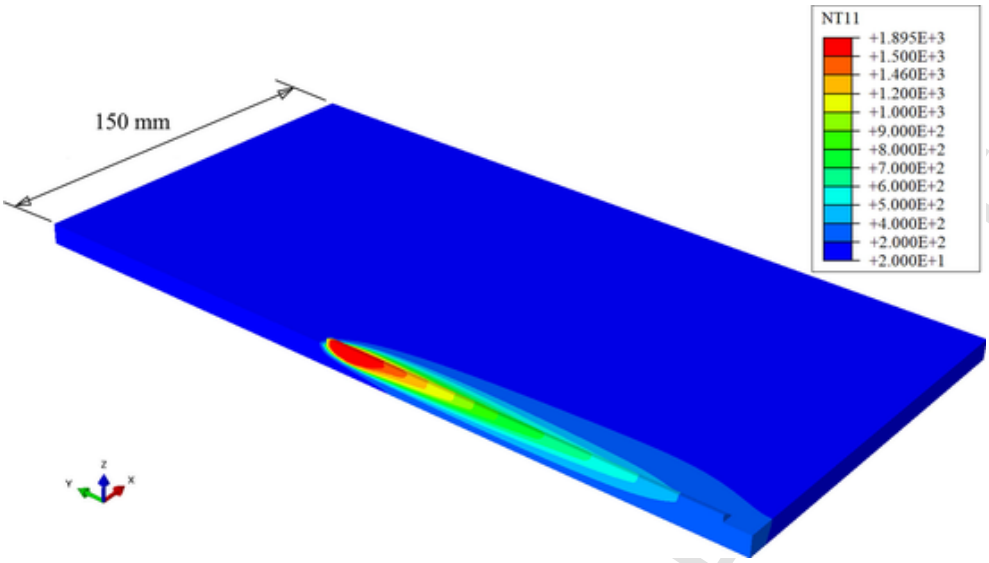

Fig. 13. Graphical presentation of thermal contours in symmetry plane during welding.

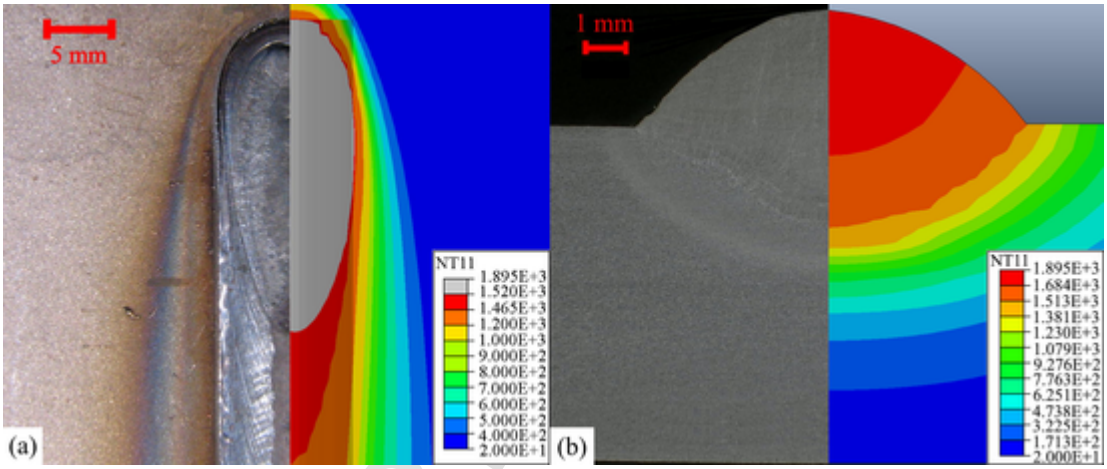

Fig. 14. Welding temperatures from simulation (NT11) and boundaries of the weld pool from simulation versus experiment on top surface (a), through thickness (b).

(a). Depth of penetration and height of weld bead from simulation and cross-section of the welded specimen at mid-section are depicted in Fig. 14 (b).

In order to validate the thermal analysis and evaluate the accuracy of developed thermal model to predict nodal transient temperatures of welding, thermal cycles at various positions on both top and bottom surfaces were determined by thermocouples. Calibration of simulated curves versus recorded temperature histories includes variation of thermal boundary conditions to match the simulated and experimental temperature fields as close as possible. This study, nevertheless, shows that calibration of thermal conductivity in different directions of the investigated material has a significant role in verification of thermal analysis. The necessity of employing anisotropic thermal conductivity rather than isotropic one in thermal analysis of welding process for the material under investigation should be corroborated. To do so, a comparison is drawn between the simulated temperature histories at certain nodes corresponding to the positions of thermocouples by the two mentioned thermal models versus the experimentally determined ones as are shown in Fig. 15.

An excellent agreement between the FE simulation results considering anisotropic thermal conductivity and measurement of peak temperatures as well as heating and cooling rates at different thermocouple positions on both top and bottom surfaces is observable. Nevertheless, obvious discrepancies exist between temperature histories predicted by the model using isotropic temperature-dependent thermal conductivity and measurements. It is needed to mention that both models are calibrated in terms of the Goldak's parameters. That is, on top surface, for two thermocouple positions T_1 and T_4, the latter located in HAZ and the former in the base metal adjacent to HAZ, as are shown in Fig. 15 (a) and (d), respectively, peak temperatures and cooling rates are predicted lower than the experiment. For two thermocouple positions far from HAZ, namely T_2 and T_3, as are respectively presented in Fig. 15 (b) and (c), simulated curves by such model yet keep distance from the experimental curves with predicted peak temperatures higher than the measured ones. The reason can be attributed to the application of incorrect pattern of thermal conduction by such model in which the energy transported in all directions are assumed to be identical.

Fig. 15 (e) and (f) unequivocally demonstrate that even more dramatic differences exist between the predicted thermal field by the model runs upon isotropic conductivity assumption and observed reality on the bottom side. Serious errors are involved in reflecting the heating rates, cooling rates and more importantly, peak temperatures when this model is put into application for this material, which proves the inability of such model to represent acceptable results concerning prediction of the temperature histories especially at the bottom surface.

The importance of accuracy in determining the temperature histories is more highlighted as it pertains to prediction of microstructure in HAZ. A close attention to Fig. 15 (d) reveals that the thermocouple position T_4 experiences temperatures higher than A_3 temperature and is fully austentitized, as is also predicted by anisotropic conductivity model, while such material point is pre-

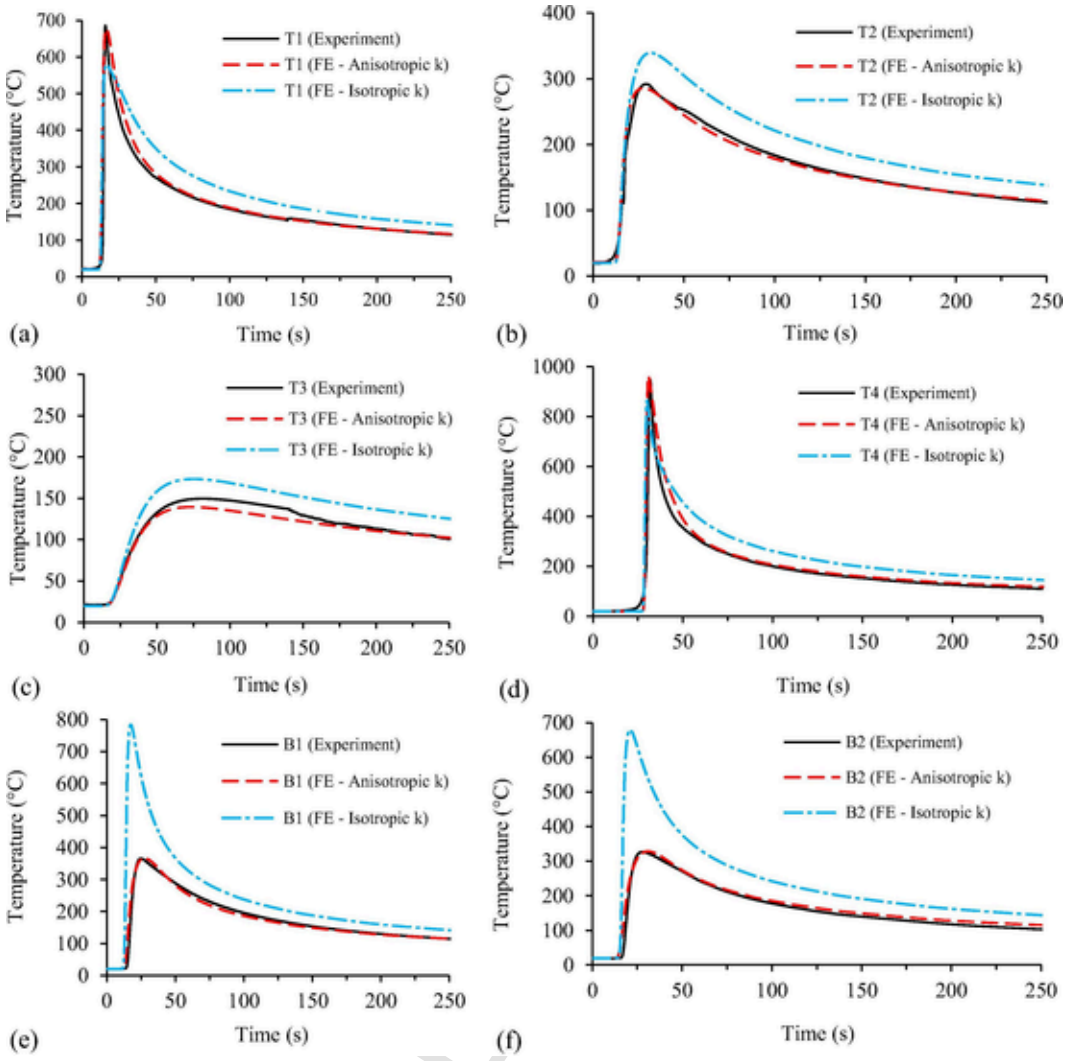

Fig. 15. Measured versus simulated (with anisotropic and isotropic thermal conductivities) temperature histories at thermocouple positions T_1 (a), T_2 (b), T_3 (c), T_4 (d), B_1 (e) and B_2 (f).

dicted to undergo incomplete austenitic transformation by the isotropic conductivity model. Another relevant example in this regard is shown in Fig. 15 (e). Based on the isotropic model, thermocouple position B_1 undergoes austenitic transformation while in fact, the temperature experienced in that material point is far lower than A_1 temperature and thus, no phase transformation is anticipated to occur in the mentioned point. Such an analysis subsequently leads to an inaccurate evaluation of the fraction of phases arising during austenite decomposition. Therefore, the reliability of the thermal analysis based on the assumption of isotropic heat conductivity for the concerned material is questionable. Validation of temperature histories is the most prominent measure of correctness and accuracy of thermo-numerical model. Such validation is the bedrock of nodal temperature transfer for subsequent metallurgical and mechanical analyses, which are highly contingent upon correct distribution of heat in FZ and HAZ.

4.2. Metallurgical analysis and prediction of microstructure

Kinetics of phase transformation as well as prediction of microstructure and boundaries of HAZ in regions whose temperatures exceeded A_1 temperature, were included in metallurgical analysis. Fig. 16 shows visual presentation of calculated volume fractions of bainite and martensite formed in HAZ and FZ upon decomposition of austenite as well as volume fraction of base material in which volume fractions of base material, bainite and martensite are presented by defined state variables SDV5, SDV7 and SDV8, respectively.

From Fig. 16 (a), for each node, volume fraction of parent material after welding and cooling can be obtained. Based on the presented figure, parent material might be untransformed (volume fraction is equal to 1 in presented contour bar), partially transformed or fully transformed (volume fraction is equal to 0 in the related contour bar). In the case of transformation of base material to austenite, in cooling stage, bainite and martensite will form whose simulated volume fractions are respectively shown in Fig. 16 (b) and (c). For an arbitrary node located 6.2 mm far from the weld center line in the mid-section of the FE model on top surface, simulated graphical presentation of welding thermal cycle and variations in volume fractions of austenite, bainite and martensite as a function of time are shown in Fig. 17.

Microstructural observation of the welded specimen in HAZ is in agreement with the results of the FE simulation with respect to the presence of a mixture of bainite and martensite, as is shown in Fig. 18. Grain growth in HAZ and prior-austenite grain boundaries with dashed lines are clearly shown in an SEM image in Fig. 18 (a). A mixture of bainite and martensite in the HAZ microstructure of the welded plate in which the volume fraction of bainite is greater than martensite volume fraction, is observable in Fig. 18 (b).

Similar to distribution of microstructure in HAZ, composition of structure in FZ, as is demonstrated in Fig. 19, consists of a bainitic microstructure in which martensite is scatteredly distributed. Martensite islands are shown with dashed lines and the letter "M" refers to martensite. Bainite share, as can be clearly seen, is larger compared to that of martensite as is also observable from the calculated fractions of bainite and martensite presented in Fig. 16.

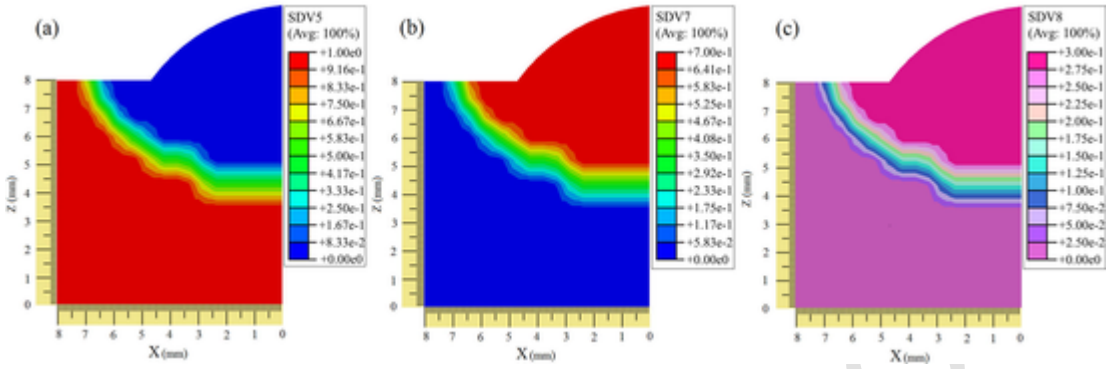

Fig. 16. Volume fractions of base metal (a), formed bainite (b) and martensite (c) in the middle section of the model.

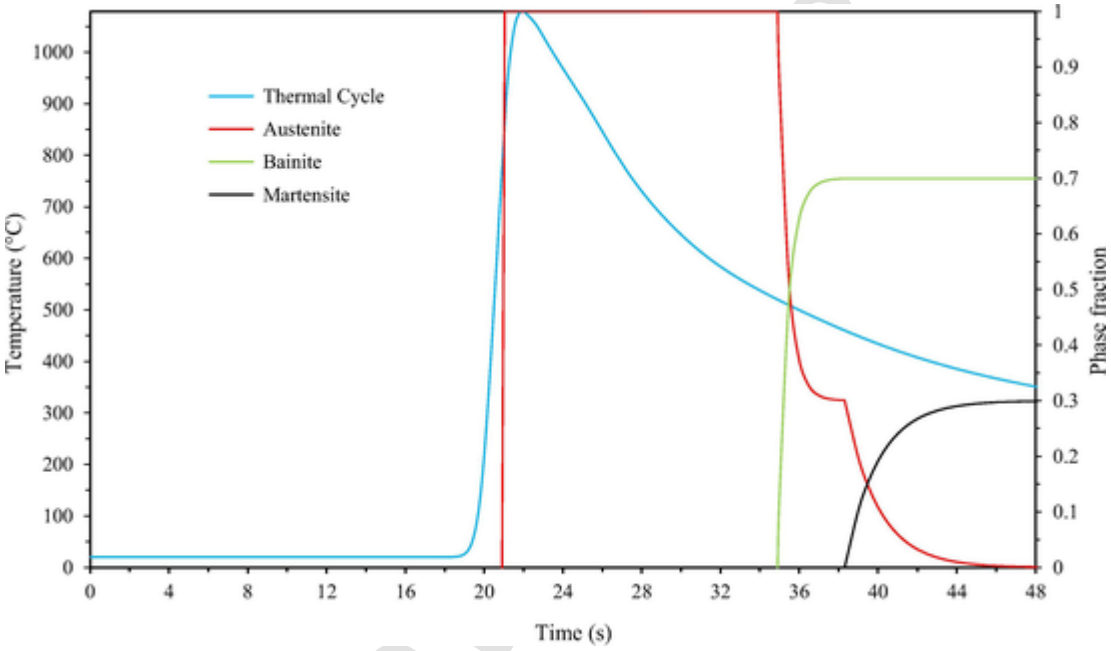

Fig. 17. Welding temperatures and volume fractions of microconstituents during the welding thermal cycle for a point in HAZ (6.2 mm from weld center line in mid-section) on top surface.

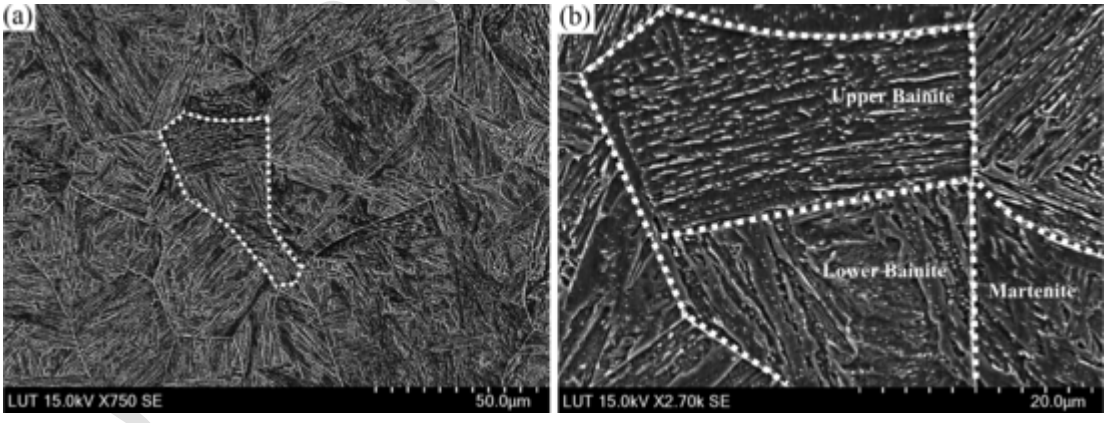

Fig. 18. SEM micrographs of HAZ, Prior austenite grain boundaries (a), a mixture of bainite and martensite (b).

4.3. Simulated mechanical analysis and the effect of SSPT on welding distortions

In order to elucidate the effect of SSPT on mechanical analysis and validation of the FE model to predict welding distortions, two simulation cases were considered. One case neglects the effect of volume change due to SSPT on mechanical analysis, while such effect was taken into account by the other model. Incorporation of SSPT in mechanical analysis was fulfilled by developing the user subroutine UEXPAN in ABAQUS in which strains were modified by including volume fractions of present phases and full volumetric change strain of each phase during heating and cooling.

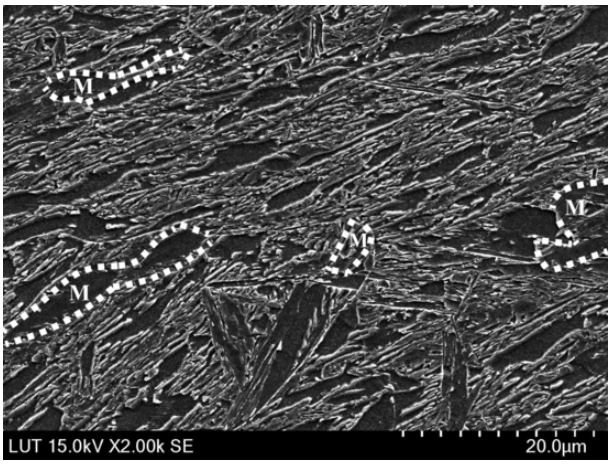

Fig. 19. SEM micrograph of FZ shows martensite with a smaller share is distributed in a bainitic microstructure.

In order to study the mesh sensitivity, four element sizes were chosen as are presented in the table 5 and mechanical analyses were performed to choose the efficient mesh to compare the results of FE models with experiment.

Table 5
Minimum element size and number of elements in each case.

Case	Min element size in weld region (length × width × thickness)	Number of meshing elements
1	5.6 × 1 × 2	7296
2	2.8 × 0.5 × 1	34,852
3	2.8 × 0.5 × 0.5	64,808
4	1.4 × 0.5 × 0.5	129,608

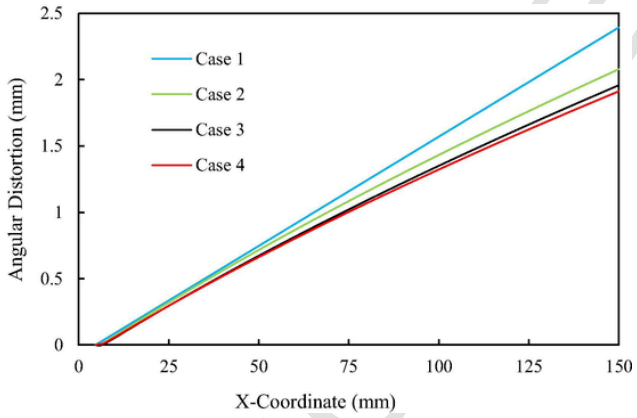

Fig. 20. Variation in angular distortion based on meshing cases.

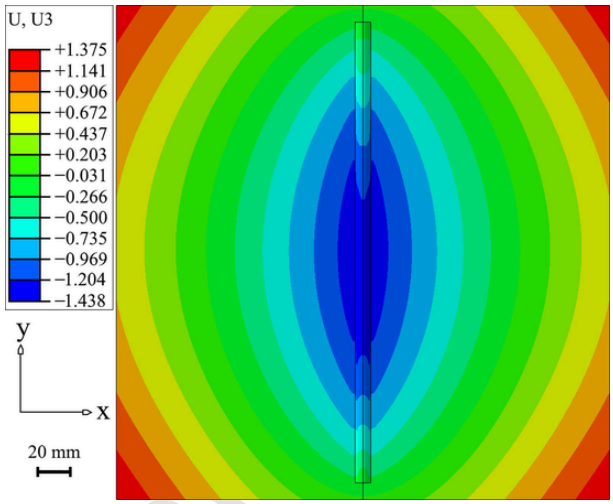

Fig. 21. Displacement contours (U3) after cooling and relaxation. (Units in mm).

The effect of element size and mesh density on angular deformation simulated by FE model considering the effect of SSPT was investigated for the cases mentioned in the table 5 and the results are plotted in Fig. 20.

As can be observed in Fig. 20, reducing the size of elements, results in decreasing the angular distortion along the path 1 (specified in Fig. 2) predicted by the FE model. The deformation decreased by 18% when the meshing style was changed from case 1 to case 3. By taking into account the accuracy and computational costs, the meshing style in case 3 was applied to the FE models. Fig. 21 shows displacement contours in which U3 values are displacement values in *Z*-direction simulated by the FE model that considers SSPT.

A comparison has been made between the results of the FE models and experimental measurements concerning out of plane displacements, namely angular and bending distortions along the defined paths on top surface of the specimen. The results of measuring angular distortion along paths 1 & 2 specified in Fig. 2, versus simulated cases (with and without SSPT) are depicted in Fig. 22 (a) and (b), respectively.

Angular distortion as is observable from Fig. 21 is symmetrical with respect to the weld center line and rises as the distance from the weld line towards the outer edges increases. The results of simulations show an acceptable agreement with measurements. The model which incorporates the effect of SSPT, however, more accurately predicts angular distortion along path 1 & 2 specified in Fig. 2, and from magnitude point of view, keeps smaller distances from the experimental ones compared to the other FE model indicating the superiority of the SSPT model. The smaller values for angular displacement predicted by the SSPT model compared to the other FE model, originate from the volume increase during bainitic and martensitic transformations resulting in smaller distortion, which is in concurrent with the findings of a study by Deng [33]. The values of bending distortion which occurs along the path 3 specified in Fig. 2, predicted by the two models are plotted versus the experimentally measured ones in Fig. 23.

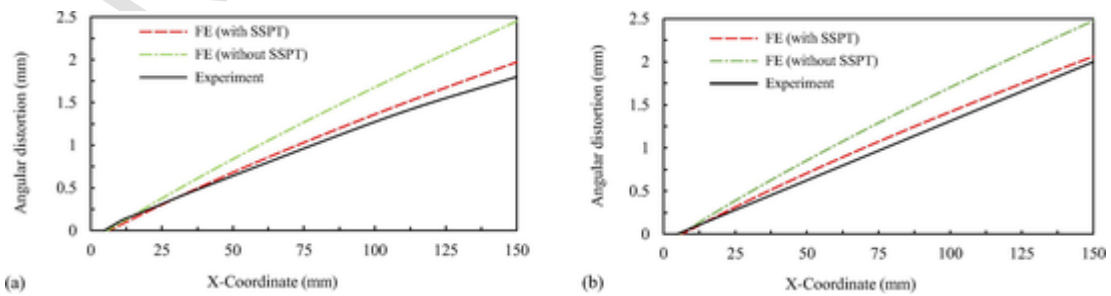

Fig. 22. Angular distortion along path 1 (a) and path 2 (b).

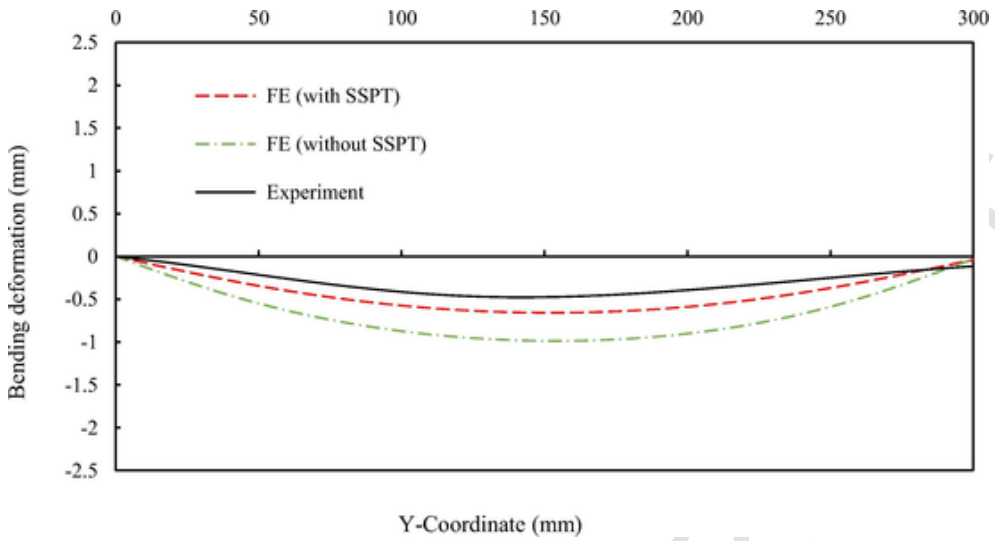

Fig. 23. Simulated bending distortion versus the experiment along the specified path.

Magnitude of bending distortion compared to the angular deformation is smaller in this study and is limited to fraction of a millimeter. Both simulated cases overpredicted out of plane bending deformation, nonetheless, the resulted curve from the model ignoring SSPT holds a large distance from the experimental one, while the values predicted by the SSPT model, sustain smaller discrepancies from the measured values which proves the SSPT model is able to provide more accuracy to the results.

5. Conclusions and future work

In this paper, a FE model to simulate bead-on-plate GMAW of an ultra-high strength carbon steel in ABAQUS was developed. A comprehensive SSPT model considering both diffusive and displacive transformations was incorporated in numerical procedure, and its effect on welding distortion patterns was investigated. FE results regarding thermal simulation and prediction of distortions were verified by experiments. The following conclusions from the simulation results and experimental measurements are drawn:

(1). The results of thermal model that uses isotropic conductivity show some differences with temperature measurement by means of thermocouples. Closer agreement between the results of thermal simulation and thermocouple measurements in terms of temperature distribution was observed when anisotropic conductivity as a calibrating tool was adopted. Based on austenite morphologies of the material and connection of grain size with heat conductivity from another research, one possible hypothesis is introduced in which reduced conductivity in thickness direction is correlated to smaller grain size through thickness.
(2). Simulation predicts that welded material in HAZ and FZ has a bainitic-martensitic microstructure in which martensite share is smaller than that of bainite. This matter is also observable from microstructural observations of welded specimen in FZ and HAZ.
(3). Prediction of welding-induced angular distortion and out of plane bending deformation with the SSPT model shows higher level of accuracy compared to the model that neglects such effect.
(4). In the present study, residual stresses are not studied. Design-wise, they are necessary to consider. Thus, in the upcoming research, numerical simulation and experimental measurement of longitudinal and transverse residual stresses will be considered.

CRediT authorship contribution statement

Mehran Ghafouri: Conceptualization, Methodology, Software, Validation, Writing - original draft, Visualization. **Joseph Ahn:** Methodology, Software, Writing - review & editing. **Juho Mourujärvi:** Validation, Writing - review & editing, Visualization. **Timo Björk:** Conceptualization, Writing - review & editing, Supervision, Funding acquisition. **Jari Larkiola:** Writing - review & editing, Supervision.

Declaration of Competing Interest

The authors declare that they have no known competing financial interests or personal relationships that could have appeared to influence the work reported in this paper.

Acknowledgements

This research was funded by Business Finland (TEKES). The CSC - IT Center for Science Ltd. is acknowledged for providing the computational resources. The support of SSAB Europe is acknowledged.

References

[1] W. Guo, L. Li, S. Dong, D. Crowther, A. Thompson Comparison of microstructure and mechanical properties of ultra-narrow gap laser and gas-metal-arc welded S960 high strength steel. Opt Lasers Eng 2017;91:1–15.
[2] W. Guo, D. Crowther, J.A. Francis, A. Thompson, Z. Liu, L. Li Microstructure and mechanical properties of laser welded S960 high strength steel. Mater Des 2015;85:534–548.
[3] D. Deng FEM prediction of welding residual stress and distortion in carbon steel considering phase transformation effects. Mater Des 2009;30(2):359–366.
[4] T. Skriko, M. Ghafouri, T. Björk Fatigue strength of TIG-dressed ultra-high-strength steel fillet weld joints at high stress ratio. Int J Fatigue 2017;94:110–120.
[5] F. Azhari, A. Heidarpour, X.-L. Zhao, C.R. Hutchinson Mechanical properties of ultra-high strength (Grade 1200) steel tubes under cooling phase of a fire: An experimental investigation. Constr Build Mater 2015;93:841–850.
[6] A. Anca, A. Cardona, J. Risso, V.D. Fachinotti Finite element modeling of welding processes. Appl Math Model 2011;35(2):688–707.
[7] J. Goldak, M. Bibby, J. Moore, R. House, B. Patel Computer modeling of heat flow in welds. Metall Trans B 1986;17(3):587–600.
[8] D. Deng, H. Murakawa Numerical simulation of temperature field and residual stress in multi-pass welds in stainless steel pipe and comparison with experimental measurements. Comput Mater Sci 2006;37(3):269–277.
[9] C. Heinze, C. Schwenk, M. Rethmeier Numerical calculation of residual stress development of multi-pass gas metal arc welding. J Constr Steel Res 2012;72:12–19.
[10] D. Deng, H. Murakawa, W. Liang Numerical simulation of welding distortion in large structures. Comput Methods Appl Mech Eng 2007;196(45–48):4613–4627.
[11] C.-H. Lee, K.-H. Chang Finite element simulation of the residual stresses in high strength carbon steel butt weld incorporating solid-state phase transformation. Comput Mater Sci 2009;46(4):1014–1022.
[12] L.-E. Lindgren Numerical modelling of welding. Comput Methods Appl Mech Eng 2006;195(48–49):6710–6736.
[13] L.-E. Lindgren Finite element modeling and simulation of welding part 1: Increased complexity. J Therm Stresses 2001;24(2):141–192.

[14] L.-E. Lindgren Finite element modeling and simulation of welding. Part 2: Improved material modeling. J Therm Stresses 2001;24(3):195–231.
[15] L.-E. Lindgren Finite element modeling and simulation of welding. Part 3: Efficiency and integration. J Therm Stresses 2001;24(4):305–334.
[16] J. Goldak, A. Chakravarti, M. Bibby A new finite element model for welding heat sources. Metall Trans B 1984;15(2):299–305.
[17] "ABAQUS user's manual, Version 2017," Dassault Systèmes®, 2017
[18] P. Suikkanen, J. Kömi Microstructure, Properties and Design of Direct Quenched Structural. Mater Sci Forum 2014;783–786:246–251.
[19] Siltanen J, Tihinen S, Kömi J. Laser and laser gas-metal-arc hybrid welding of 960 MPa direct-quenched structural steel in a butt joint configuration. J Laser Appl. 2015;27(S2): S29007-1-8.
[20] T. Björk, J. Toivonen, T. Nykänen Capacity of Fillet Welded Joints Made of Ultra High-Strength Steel. Welding World 2012;56(3–4):71–84.
[21] M. Amraei, T. Skriko, T. Björk, X.-L. Zhao Plastic strain characteristics of butt-welded ultra-high strength steel (UHSS). Thin-Walled Struct 2016;109:227–241.
[22] SSAB, Welding Handbook, SSAB, Oxelösund, 2016.
[23] M. Kubiak, W. Piekarska Comprehensive model of thermal phenomena and phase transformations in laser welding process. Comput Struct 2016;172:29–39.
[24] C.-H. Lee, K.-H. Chang Prediction of residual stresses in high strength carbon steel pipe weld considering solid-state phase transformation effects. Comput Struct 2011;89(1–2):256–265.
[25] J. Ahn, E. He, L. Chen, R. Wimpory, J. Dear, C. Davies Prediction and measurement of residual stresses and distortions in fibre laser welded Ti-6Al-4V considering phase transformation. Mater Des 2017;115:441–457.
[26] JMatPro,Version 8.0, Sente Software Ltd.
[27] Y. Danis, E. Lacoste, C. Arvieu Numerical modeling of inconel 738LC deposition welding: Prediction of residual stress induced cracking. J Mater Process Technol 2010;210(14):2053–2061.
[28] A.A. Bhatti, Z. Barsoum, H. Murakawa, I. Barsoum Influence of thermo-mechanical material properties of different steel grades on welding residual stresses and angular distortion. Mater Des 2015;65:878–889.
[29] A. Yaghi, T. Hyde, A. Becker, W. Sun, J. Williams Residual stress simulation in thin and thick-walled stainless steel pipe welds including pipe diameter effects. Int J Press Vessels Pip 2006;83(11–12):864–874.
[30] B. Brickstad, B. Josefson A parametric study of residual stresses in multi-pass butt-welded stainless steel pipes. Int J Press Vessels Pip 1998;75(1):11–25.
[31] T. Lauwagie, H. Sol, G. Roebben, W. Heylen, Y. Shi, O. Van der Biest Mixed Numerical-Experimental Identification of Elastic Properties of Orthotropic Metal Plates. NDT E Int 2003;36(7):487–495.
[32] P. Jonšta, I. Vlčková, Ľ. Krišták, I. Špička, Z. Jonšta Contribution to the Thermal Properties of Selected Steels. Metalurgija 2015;54(1):187–190.
[33] M. Chiumenti, M. Cervera, A. Salmi, C. Agelet de Saracibar, N. Dialami, K. Matsui Finite element modeling of multi-pass welding and shaped metal deposition processes. Comput Methods Appl Mech Eng 2010;199:2343–2359.
[34] A.A. Bhatti, Z. Barsoum, M. Khurshid Development of a finite element simulation framework for the prediction of residual stresses in large welded structures. Comput Struct 2014;133:1–11.
[35] H. Li, K. Gai, L. He, C. Zhang, H. Cui, M. Li Non-Isothermal Phase-Transformation Kinetics Model for Evaluating the Austenization of 55CrMo Steel Based on Johnson–Mehl–Avrami Equation. Mater Des 2016;92:731–741.
[36] W. Piekarska, M. Kubiak, Z. Saternus Numerical Modelling of Thermal and Structural Strain in Laser Welding Process. Arch Metall Mater 2012;57(4):1219–1227.
[37] Y. Li, H. Lu, C. Yu, Y. Wu Accurate Prediction of Welding Stress Evolution by Considering Improved Phase Transformation Model. Mater Trans 2015;56(5):715–719.
[38] A. Yaghi, T. Hyde, A. Becker, J. Williams, W. Sun Residual stress simulation in welded sections of P91 pipes. J Mater Process Technol 2005;167(2–3):480–487.
[39] X. Shan, C. Davies, T. Wangsdan, N. O'Dowd, K. Nikbin Thermo-mechanical modelling of a single-bead-on-plate weld using the finite element method. Int J Press Vessels Pip 2009;86(1):110–121.
[40] J. Ahn, E. He, L. Chen, T. Pirling, J. Dear, C. Davies Determination of residual stresses in fibre laser welded AA2024-T3 T-joints by numerical simulation and neutron diffraction. Mater Sci Eng, A 2018;712:685–703.
[41] G. Mi, L. Xiong, C. Wang, X. Hu, Y. Wei A thermal-metallurgical-mechanical model for laser welding Q235steel. J Mater Process Technol 2016;238:39–48.
[42] B. Taljat, B. Radhakrishnan, T. Zacharia Numerical analysis of GTA welding process with emphasis on post-solidification phase transformation effects on residual stresses. Mater Sci Eng, A 1998;246(1–2):45–54.
[43] L.-E. Lindgren Computational Welding Mechanics. Cambridge: Woodhead Publishing; 2007.
[44] X. Zhu, Y. Chao Effects of temperature-dependent material properties on welding simulation. Comput Struct 2002;80(11):967–976.
[45] M. Dabiri, M. Lindroos, T. Andersson, S. Afkhami, A. Laukkanen, T. Björk Utilizing the theory of critical distances in conjunction with crystal plasticity for low-cycle notch fatigue analysis of S960 MC high-strength steel. Int J Fatigue 2018;117:257–273.
[46] M. Dabiri, M. Isakov, T. Skriko, T. Björk Experimental fatigue characterization and elasto-plastic finite element analysis of notched specimens made of direct-quenched ultra-high-strength steel. Proc Inst Mech Eng, Part C: J Mech Eng Sci 2016;231(22):4209–4226.
[47] J. Goldak, M. Akhlaghi Computational Welding Mechanics. New York: Springer; 2005.
[48] D. Deng, H. Murakawa Finite element analysis of temperature field, microstructure and residual stress in multi-pass butt-welded 2.25Cr–1Mo steel pipes. Comput Mater Sci 2008;43(4):681–695.
[49] D.A. Porter, K.E. Easterling, M.Y. Sherif Phase Transformation in Metals and Alloys. Boca Raton: CRC Press; 2009.